

Designing a double-coated cathode with high entropy oxides by microwave-assisted hydrothermal synthesis for highly stable Li–S batteries

*Original*

Designing a double-coated cathode with high entropy oxides by microwave-assisted hydrothermal synthesis for highly stable Li–S batteries / Colombo, R.; Garino, N.; Versaci, D.; Amici, J.; Para, M. L.; Quartarone, E.; Francia, C.; Bella, F.; Bodoardo, S.. - In: JOURNAL OF MATERIALS SCIENCE. - ISSN 0022-2461. - ELETTRONICO. - 57:33(2022), pp. 15690-15704. [10.1007/s10853-022-07625-7]

*Availability:*

This version is available at: 11583/2971395 since: 2022-09-18T15:27:05Z

*Publisher:*

SPRINGER

*Published*

DOI:10.1007/s10853-022-07625-7

*Terms of use:*


This article is made available under terms and conditions as specified in the corresponding bibliographic description in the repository

*Publisher copyright*

(Article begins on next page)



# Designing a double-coated cathode with high entropy oxides by microwave-assisted hydrothermal synthesis for highly stable Li–S batteries

Roberto Colombo<sup>1</sup>, Nadia Garino<sup>2</sup>, Daniele Versaci<sup>1</sup>, Julia Amici<sup>1,\*</sup> , Maria Laura Para<sup>1</sup>, Eliana Quartarone<sup>3</sup>, Carlotta Francia<sup>1</sup>, Federico Bella<sup>1</sup>, and Silvia Bodoardo<sup>1</sup>

<sup>1</sup>Electrochemistry Group, Department of Applied Science and Technology, Politecnico di Torino, C.so Duca degli Abruzzi 24, 10129 Turin, Italy

<sup>2</sup>Materials and Processes for Micro and Nano Technologies Group, Department of Applied Science and Technology, Politecnico di Torino, C.so Duca degli Abruzzi 24, 10129 Turin, Italy

<sup>3</sup>Department of Chemistry, INSTM, University of Pavia, Via Taramelli 16, 27100 Pavia, Italy

Received: 13 May 2022

Accepted: 8 August 2022

© The Author(s) 2022

## ABSTRACT

Nowadays, Li–S batteries are considered as one of the most promising alternatives to Li-ion technology in the near future, thanks to their high specific capacity and their significantly lower environmental impact and production costs. Consequently, many efforts have been directed to tackle with the inherent issues that affect Li–S batteries. One of the main problems is the so-called shuttle effect, which basically entails the unwanted migration of lithium polysulfides (LiPSs) from the cathode to the anode side, causing the degradation of the cell. Here, we report an effective strategy to restrain the shuttle effect and increase the kinetics at the cathode of the lithium–sulfur (Li–S) battery. A functional layer including high entropy oxides (HEO) coated onto the sulfur cathode allows to exploit the HEOs capability as promoter catalysts for the conversion of LiPSs. Pure HEO powders are synthesized by fast, highly efficient microwave irradiation, followed by heat treatment at 930 °C. The formation of highly crystalline HEO is confirmed by X-ray diffraction analysis. The LiPSs adsorption capability of HEO is evaluated by UV–vis and X-ray photoelectron spectroscopy analyses. The effect of the HEO-coated sulfur cathode on the electrochemical performance of the Li–S battery is studied by cyclic voltammetry and galvanostatic charge/discharge. The cell with double-coated cathode delivers an initial discharge capacity of 1173 mAh/g at C/10 with 45% capacity retention over 500 cycles at C/5, approaching ~ 99% coulombic efficiency.

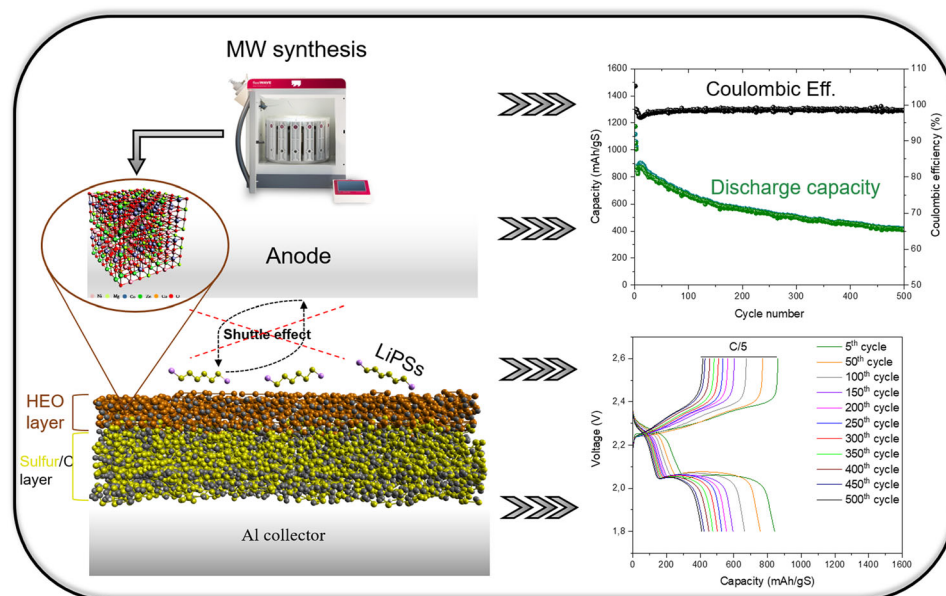
Handling Editor: David Cann.

Address correspondence to E-mail: [julia.amici@polito.it](mailto:julia.amici@polito.it)

<https://doi.org/10.1007/s10853-022-07625-7>

Published online: 23 August 2022

## GRAPHICAL ABSTRACT



## Introduction

The lithium–sulfur (Li–S) battery is a promising technology for electrochemical energy storage, and its key contribution is the high gravimetric energy density that can be achieved with the sulfur cathode and the lithium anode. Based on the overall redox reaction  $\text{S}_8 + 16 \text{Li}^+ + 16 \text{e}^- \leftrightarrow 8 \text{Li}_2\text{S}$ , the practical energy density of the Li–S battery is around 25–33% of the theoretical value (2600 Wh/kg), which is still 2–3 times higher than the best-performing Li-ion battery (LIB) [1]. The sulfur cathode is also a friendly option in terms of safety and sustainability and, due to its abundance and low price, in fact the cost of the Li–S battery is estimated to be lower than 100 \$/kWh, compared to 150 \$/kWh for current LIBs [2]. Despite these advantages, implementation of the Li–S battery is required to overcome the poor power capability and short cycle life due to gradual capacity fading [3]. The drawbacks arise from the complex working mechanism at cell level, where the solid product of the discharge reaction ( $\text{Li}_2\text{S}$ ) is accompanied by formation of various lithium polysulfides (LiPSs) intermediates that can be either soluble or insoluble in the

organic electrolyte, depending on the length of the chain. This entails that soluble LiPSs may diffuse to lithium metal, where they are reduced to lower LiPSs chain, causing anode corrosion and low coulombic efficiency, and may diffuse back to the sulfur cathode in a process known as “shuttle mechanism.” [4] The diffusion of LiPSs induces the redistribution of insulating  $\text{Li}_2\text{S}$  on the conductive carbon particles at the cathode, resulting in the passivation of the active surface and large overpotential for the sulfur redox conversion [5, 6].

To address these problems, nanostructured carbon hosts [7] combined with oxides/sulfides materials [8] have been employed to improve the electrochemical performance of Li–S batteries. At the same time, another approach consists of adding multifunctional interlayers in the traditional cell configuration, in order to reduce the shuttle effect creating a barrier able to retain LiPSs through physiochemical adsorption [9–11]. Although these strategies greatly improved the capacity and cycle life of Li–S cells, the complicated synthesis processes of some nanostructured materials prevent their upscaling for commercial applications [12]; moreover, in some cases, the integration of interlayers is still difficult in practical

continuous production and involves additional costs [13]. As an alternative approach to stabilize LiPSs within the cathode [14], that could be easily scaled in the continuous roll-to-roll process, is the two-step coating technique. In this cathode modification strategy, a second layer is coated onto the top of the dried sulfur-containing electrode [15]. As a result, a double-coating containing metal oxides [13] can both enable adsorption of the soluble LiPSs and enhance the kinetics of transformation processes of LiPSs to  $\text{Li}_2\text{S}/\text{Li}_2\text{S}_2$  [16, 17] increasing long-term performances and battery lifetime.

Concerning metal oxides, polar multicomponent metal oxides have been recently developed to restrain LiPSs dissolution and migration by chemical immobilization. Compared to the single counterparts, the benefit of multicomponent metal oxides lies on the fact that they have more oxygen vacancies and active sites, along with variable and high valence transition metal ions that enhance the surface interactions with LiPSs and promote their conversion [18]. This usually results in high specific capacity and/or excellent capacity retention during cell cycling. Xiong et al. [19] reported that  $\text{ZnCo}_2\text{O}_4$  particles supported on N-doped reduced graphene oxide sheets could host up to 82% of sulfur. The composite cathode was able to deliver 645 mAh/g and maintained 71% of the initial capacity after 200 cycles at 1600 mA/g. Reversible specific capacities of 1350 and 900 mAh/g were achieved at rates of 0.1 and 1C, respectively, with ternary carbon nanotubes (CNT)/ $\text{NiFe}_2\text{O}_4$ -S hybrid materials in which CNT enhanced the conductivity, and the 2D  $\text{NiFe}_2\text{O}_4$  nanosheets were used for LiPSs immobilization [20]. Novel  $\text{Li}_2\text{S}@\text{LiTiO}_2$  core-shell nanocomposites enabled rapid conversion of longer chain (highly soluble) LiPSs to short ones, which exhibited minimum solubility in the electrolyte and prevented the lithium anode from corrosion [21], while nanosized  $\text{Mg}_{0.6}\text{Ni}_{0.4}\text{O}$  enhanced the electrochemical kinetics of sulfur/poly(acrylonitrile) composites, resulting in reduced cathode polarization [22]. Due to the features of multicomponent oxides, high-entropy oxides characterized by a single-phase oxide system with several cations provide strong polar surface to chemically adsorb the sulfur. Recently, Zheng et al. [23] encapsulated S in high entropy oxide (HEO), in order to immobilize LiPSs directly in the cathode. The HEO was the rock-salt type  $(\text{Co}_{0.2}\text{Cu}_{0.2}\text{Mg}_{0.2}\text{Ni}_{0.2}\text{Zn}_{0.2})\text{O}$  system with five different metal cations [24], which has also gained

interest as anode material in LIBs [25–27]. Nonetheless, HEO has been successfully employed as coating of NMC811 cathode active material. In this case, the HEO coating acted as an artificial cathode electrolyte interphase (CEI) that inhibited side reactions at the cathode/electrolyte interface, significantly reducing the polarization of the Li-ion battery and increasing the rate of the capacity retention [28].

In the Li-S battery, the homogeneous distribution of multiple metal active sites of  $(\text{Co}_{0.2}\text{Cu}_{0.2}\text{Mg}_{0.2}\text{Ni}_{0.2}\text{Zn}_{0.2})\text{O}$  accelerates the redox reaction kinetics of LiPSs. First-principle calculations based on density functional theory (DFT) applied to the multicomponent HEO- $\text{Li}_2\text{S}_6$  model enlightened a decrease in both Li-O and S-Ni bond distances compared to those of monometallic  $\text{NiO}@\text{Li}_2\text{S}_6$  model, suggesting a stronger affinity between the LiPSs and the multiple metal species in the HEO structure [23]. Similarly, Gao et al. [29] used  $(\text{Mg}_{0.2}\text{Mn}_{0.2}\text{Ni}_{0.2}\text{Co}_{0.2}\text{Zn}_{0.2})\text{Fe}_2\text{O}_4$  HEO nanofibers produced by electrospinning as catalytic host of sulfur and demonstrated fast kinetics of nucleation/growth of  $\text{Li}_2\text{S}$  during cell charging. The chemical adsorption of LiPSs on HEO nanofibers was demonstrated by XPS, UV analyses and electrochemical tests confirmed their catalytic activity in the conversion reaction. In this case, the S/HEO composite was prepared by combining sulfur with the host HEO via melt infusion at 155 °C for 12 h in Ar-filled autoclave, which is still the most general synthesis technique for the sulfur composite so far. Once melted, sulfur soaks in the host pore by capillarity and then creates nanocrystals bonded to the host material during cooling. However, agglomeration of S on the external surface cannot be avoided, and this sulfur is still easily dissolved in electrolytes. This could be an issue, especially during long cycling at low C rates.

In the present work, the benefits of HEO-double-coated cathode are demonstrated. Sulfur is simply mixed with carbon black (KJB) and the binder, avoiding its confinement inside the porosity of the host matrix, which means an unfavorable condition for preventing LiPSs shuttling. By building the dual-layer cathode, in which the sulfur/carbon active material is sandwiched between the aluminum current collector and the  $(\text{Co}_{0.2}\text{Cu}_{0.2}\text{Mg}_{0.2}\text{Ni}_{0.2}\text{Zn}_{0.2})\text{O}$  HEO layer, the capacity is greatly improved and the Li-S cell can retain almost 46% of the initial capacity after 500 cycles at moderate C/5 cycling rate.

Finally, as far as high entropy oxides are concerned, there are several processing routes to obtain them [30]. As a matter of fact, the typical solid-state synthesis [24, 31, 32] of HEO requires very long ball milling time to achieve homogeneous distribution of the different oxides precursors prior to calcination. Although the calcination step is necessary, a new method for HEO preparation has been explored here, which is efficient in saving time and energy [33, 34]. In this work, the hydrothermal synthesis route is adapted with the microwave one, since the latter requires a shorter reaction time (1 h vs. 1 day) [35]. Indeed, the traditional hydrothermal method [36, 37] offers a similar approach since it consists of two steps: a first one in which the precursors solution is heated for a long time (ranging from 5 h to 2 days) inside a steel vessel and a second step which is essentially the calcination at higher temperature (above 900 °C). Compared to this method, microwave synthesis can drastically reduce the time and the energy required to obtain the intermediate powders that are then calcined in the second step, in addition to allowing a better control over the precursor synthesis and its homogeneity thanks to a more homogenous heating process.

Microwave-assisted hydrothermal synthesis is also safer than flame pyrolysis [38] and allows higher products reproducibility [34, 34]. Therefore, it is believed that these cost-effective and easy techniques for both HEO and sulfur cathode preparations can enable to build better and cheaper Li-S batteries and open up new avenues to the use of high-entropy materials in energy conversion and storage devices.

## Experimental section

### (Co<sub>0.2</sub>Cu<sub>0.2</sub>Mg<sub>0.2</sub>Ni<sub>0.2</sub>Zn<sub>0.2</sub>)O HEO synthesis

Nickel sulfate hexahydrate (NiSO<sub>4</sub>·6H<sub>2</sub>O; Merck), copper sulfate pentahydrate (CuSO<sub>4</sub>·5H<sub>2</sub>O; Merck), magnesium sulfate heptahydrate (MgSO<sub>4</sub>·7H<sub>2</sub>O; Merck), cobalt sulfate heptahydrate (CoSO<sub>4</sub>·7H<sub>2</sub>O; Merck) and zinc sulfate heptahydrate (ZnSO<sub>4</sub>·7H<sub>2</sub>O; Merck) were used as nickel, copper, magnesium, cobalt and zinc precursors, respectively. Equimolar amounts of the metal salts were separately dissolved in deionized water to obtain 0.02 M solutions. Then, 40 mL of the aqueous salt solution (0.1 M) was added to 10 mL sodium hydroxide NaOH solution (1.2 M)

and was magnetically stirred for 15 min. Subsequently, the solution was placed in the microwave oven (Milestone flexiWAVE) and exposed to microwave irradiation at 130 °C for 1 h, with a heating time of 5 min (21 °C/min). The solution was then centrifuged at 7000 rpm (by Thermo Scientific SL16 centrifuge, Thermo Fisher) to separate the precipitated powder from the solution. The powder was washed several times with deionized water and ethanol (Aldrich). After drying, the powder was treated at 930 °C, in air, for 5 h.

### Structural-morphological characterization of HEO material

X-ray diffraction (XRD) analysis was carried out by a PANalytical X'Pert (Cu K $\alpha$  radiation) diffractometer. Data were collected with a 2D solid-state detector (PIXcel) from 10 to 90° (2 $\theta$ ) with a step size of 0.026° (2 $\theta$ ) and a wavelength of 1.54187 Å.

Field emission scanning electron microscopy (FESEM) analysis was carried out by Zeiss SUPRA<sup>TM</sup> 40 with Gemini column and Schottky field emission tip (tungsten at 1800 K). Acquisitions were made at acceleration voltage of 3 kV and working distance between 2.1 and 8.5 mm, with magnification up to 1000 kX. Transmission electron microscopy (TEM) analysis was performed by High-Resolution JEOL 300 kV.

The Brunauer–Emmett–Teller (BET) specific surface area (SSA) was determined by nitrogen physisorption at 77 K using a Micrometrics ASAP 2020 instrument. The specific surface area was calculated with the BET model in the relative pressure range of 0.07–0.30 by assuming 0.162 nm<sup>2</sup>/molecule as the molecular area of nitrogen.

X-ray photoelectron spectroscopy (XPS) measurements were carried out using a PHI Model 5000 electron spectrometer equipped with an aluminum anode (1486 eV) monochromatic source, with a power of 25.0 W and high-resolution scan with 11.75 eV pass energy. The instrument typically operates at pressures below 5 × 10<sup>−8</sup> mbar.

For LiPSs adsorption tests, a Li<sub>2</sub>S<sub>6</sub> solution was prepared by mixing sulfur and Li<sub>2</sub>S at a molar ratio of 5:1 in 1,2-dimethoxyethane (DME) and 1,3-dioxolane (DOL) (1:1 by volume) for 72 h at 70 °C, under continuous stirring in argon atmosphere; all chemicals were purchased from Sigma-Aldrich. Then, the resulting brownish-red Li<sub>2</sub>S<sub>6</sub> solution was diluted to



1.0 mM for LiPSs adsorption test, and then, 50 mg of HEO was dispersed into such solution. The mixture was left to interact for 12 h. Then, the solid product (HEO +  $\text{Li}_2\text{S}_6$ ) was filtered and dried in glove box prior to XPS analysis.

The  $\text{Li}_2\text{S}_6$  solutions were loaded into quartz cuvette sample holders inside the argon-filled glove box, then sealed and placed in closed vials. The vials were brought out of the glove box to the Jenway 6850 double beam spectrophotometer for UV-vis analysis.

### Double-coated cathode preparation, cell assembly and electrochemical tests

All the working electrodes were prepared by solvent tape casting method. The slurry for the “standard” S cathode (STD) was prepared using sulfur, Ketjen-black® carbon (KB, EC-300 J, AkzoNobel) and poly(vinylidene difluoride) (PVdF, Arkema) in *N*-methyl-2-pyrrolidinone (Sigma-Aldrich). The STD electrode composition was set at 70:20:10 by weight. Prior to casting, the slurry was ball milled at 30 Hz for 15 min, using two zirconia spheres with a radius of 0.25 cm, by a Retsch® MM40 ball miller. The slurry was then deposited on the aluminum current collector by doctor blade technique. The blade was adjusted at 200  $\mu\text{m}$  deposition by the automatic film applicator (Sheen 1133 N) with a speed of 50  $\text{mm s}^{-1}$ . After coating, the electrode was dried at 50 °C for 90 min. For the second layer coating, the selected ratio adopted between HEO, KB and PVDF was: 90:0:10 and 80:10:10, respectively, named as STD + HEO90 and STD + HEO80. The blade was adjusted at 200  $\mu\text{m}$  deposition. After solvent evaporation at 50 °C for 90 min, disks of 1.76  $\text{cm}^2$  were punched out, vacuum dried at 40 °C for 4 h (in Büchi Glass Oven B-585), and then transferred into an argon-filled dry glove box (MBraun Labstar,  $\text{H}_2\text{O}$  and  $\text{O}_2$  content < 1 ppm) for cell assembly. In the double-coated cathode, sulfur loading was 1.0  $\text{mg/cm}^2$ .

The electrodes were assembled in 2032 coin-type cells with lithium disk (Chemetall Foote Corporation, Ø 16 mm) as counter electrode and Celgard 2500 separator, (25  $\mu\text{m}$  thickness, Ø 19 mm). The electrolyte was a solution of DME and DOL 1:1 (v/v) with 1.0 M lithium bis(trifluoromethanesulfonyl)imide ( $\text{CF}_3\text{SO}_2\text{N}(\text{LiSO}_2\text{CF}_3)_2$ , LiTFSI, Sigma-Aldrich) and 0.25 M lithium nitrate ( $\text{LiNO}_3$ , Sigma-Aldrich). The solution was stored in the glove box 12 h prior to use. The electrolyte amount never

exceeded 10  $\mu\text{L}$  per mg of sulfur. The cell cycling performances were investigated by galvanostatic discharge/charge cycling (GC) using an Arbin LBT-21084 battery tester at room temperature. GC tests were carried out in the potential range of 1.8–2.6 V versus  $\text{Li}^+/\text{Li}$  at different current regimes. The C-rate was calculated with respect to the theoretical capacity of sulfur (1672  $\text{mAh/g}$ ). For cyclic voltammetry (CV), the electrode potential was reversibly scanned from 1.7 to 2.8 V versus  $\text{Li}^+/\text{Li}$  at different scan rates using a Biologic 092-11/2e potentiostat/galvanostat. Electrochemical impedance spectroscopy (EIS) was performed in coin cells to analyze the time-dependent processes that occur on the standard (STD) and modified cathodes (HEO80 and HEO90), the responses were recorded before and after eight CV cycles. The impedance was measured at OCV from  $10^5$  to  $5 \times 10^{-3}$  Hz, with a 10 mV amplitude perturbation, and the CV was performed at 0.05  $\text{mV/s}$  from 1.7 to 2.8 V.

## Results and discussion

### Morphological characterization of HEO material

HEO was prepared by hydrothermal-assisted microwave method, followed by thermal treatment in air; the XRD patterns of the synthesized powders before and after calcination are detailed in Fig. 1a. The presence of clear peaks indicated that at least a fraction of the powder obtained by microwave irradiation is crystalline. Two specific crystalline phases can be recognized in the sample, which are  $\text{Co}(\text{OH})_2$  (card no. 98-002-6763, hexagonal, marked as ♦) and  $\text{ZnO}$  (card no. 98-002-6170, marked as •); nevertheless, the presence of brucite  $\text{Mg}(\text{OH})_2$  and  $\text{Ni}(\text{OH})_2$  phases cannot be excluded since their XRD reflexes are partially overlapped with those associated with the identified phases. After calcination at 900 °C, the XRD characteristic peaks of the hydroxide disappeared, but the XRD pattern was still multiphasic. The diffraction peaks at  $2\theta$  values of 36.8, 42.7, 62.0, 74.1, 78.2 are indicative of (111), (200), (220), (311) and (222) planes of the rocksalt crystal structure ( $\text{CoCuMgNiZnO}$  HEO (peaks marked as ♣, space group  $Fm-3m$ ) [39], but small peaks due to hexagonal  $\text{ZnO}$  are also observed. At the calcination temperature of 930 °C, the formation of the single rock salt

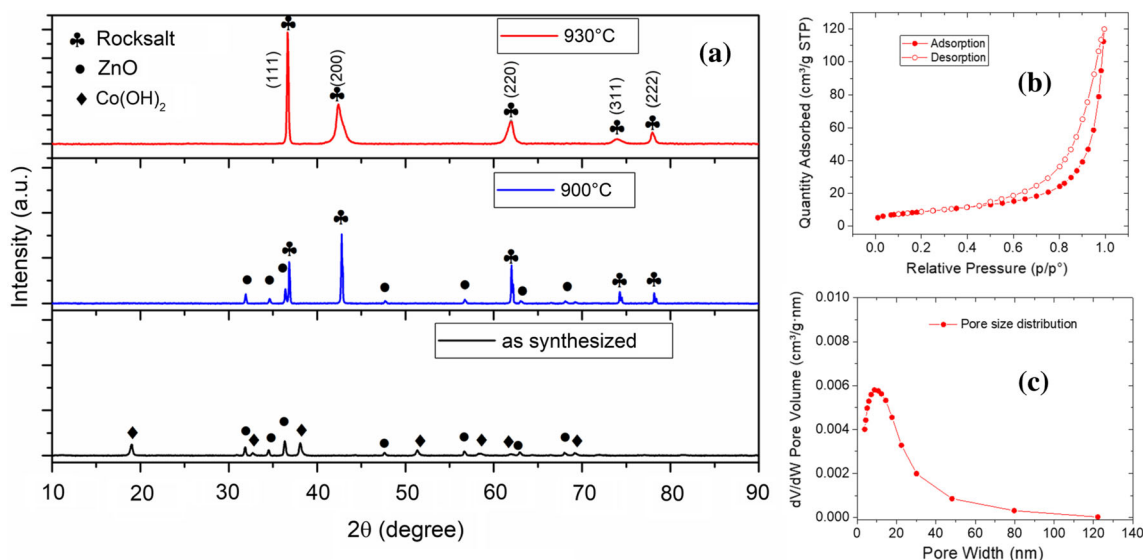


**Figure 1** **a** XRD analysis of the sample obtained by microwave irradiation at 130 °C for 1 h (black pattern), after calcination in air at 900 °C (blue) and at 930 °C (red); **b** N<sub>2</sub> adsorption/desorption isotherms of HEO and **c** the pore size distribution graph.

structure was complete. No trace of ZnO was detected in the diffraction pattern at 930 °C.

Additionally, it is interesting to note that the relative intensity of the main peaks, (111) and (200), of the experimental spectra reported in Fig. 1a is reversed with respect to the theoretical one of the rocksalt structure: Commonly, the peak representative of the (200) plane is higher than the one associated with the (111) plane. Moreover, the XRD pattern shows an evident peak broadening of the (200), (220) and (311) reflections, but this does not happen for (111) and (222) reflections. This could be due to anisotropy in the crystallite size or to anisotropic lattice disorder, which is a recurring event in HEO materials as a result of the displacements of the cation/oxygen in the lattice with respect to their ideal position. As observed by Berardan et al. [40], the deviation from the ideal rocksalt structure mostly depends on the thermal history of the sample, and the broadening along the (200), (220) and (311) reflections can be ascribed to higher cationic site density along these crystallographic planes [35].

N<sub>2</sub> adsorption/desorption analysis (Fig. 1b) of HEO shows a type IV isotherm [41], with pore size distribution that highlights the existence of mesopores (Fig. 1c), with a cumulative pore volume being 0.0847 cm<sup>3</sup>/g. The BET SSA is 32.29 m<sup>2</sup>/g, which is consistent to BET values of HEO obtained via mechanical ball milling [23]. The SSA might be an additional factor in stabilizing the cell capacity

through surface adsorption of LiPSs, although here it plays a minor role than the chemical interaction [42] because the value is rather low.

FESEM analysis was performed to assess the structural morphology of HEO, and the results are shown in Fig. 2. HEO is composed of aggregated grains of particles with irregular shape exhibiting a range of size from nano- to microparticles, with well-distributed small pores located at the grain boundaries (Fig. 2a) and similar in morphology and size to those obtained by hydrothermal synthesis [35]. From Fig. 2b, the average particle size distribution is within the range of 0.5–1.5 μm, although some abnormal elongated grains of larger size can be also detected.

Energy-dispersive X-ray spectroscopy (EDX) mapping of HEO showed the presence of the five elements throughout the whole structure. The EDX signals for the Kα emission energies (Fig. 3b–f) of Mg, Ni, Zn, Co and Cu appear as homogeneous distribution throughout the entire sample at the micrometer level, confirming the chemical and microstructural homogeneity. Moreover, the average atomic composition of O, Mg, Co, Ni, Cu and Zn in HEO is 49.43%, 9.43%, 9.80%, 9.19%, 9.45% and 12.7%, respectively, which is nearly equiatomic among the metals (Fig. 3h), with no particular element segregation on the surface of the sample. TEM micrographs (Fig. 3g, i) show that the as-synthesized powder presents lattice fringes, and the average distance spacing between adjacent lattice planes is

**Figure 2** **a** FESEM analysis of the HEO sample after calcination at 930 °C; **b** FESEM micrograph of HEO at higher magnification.

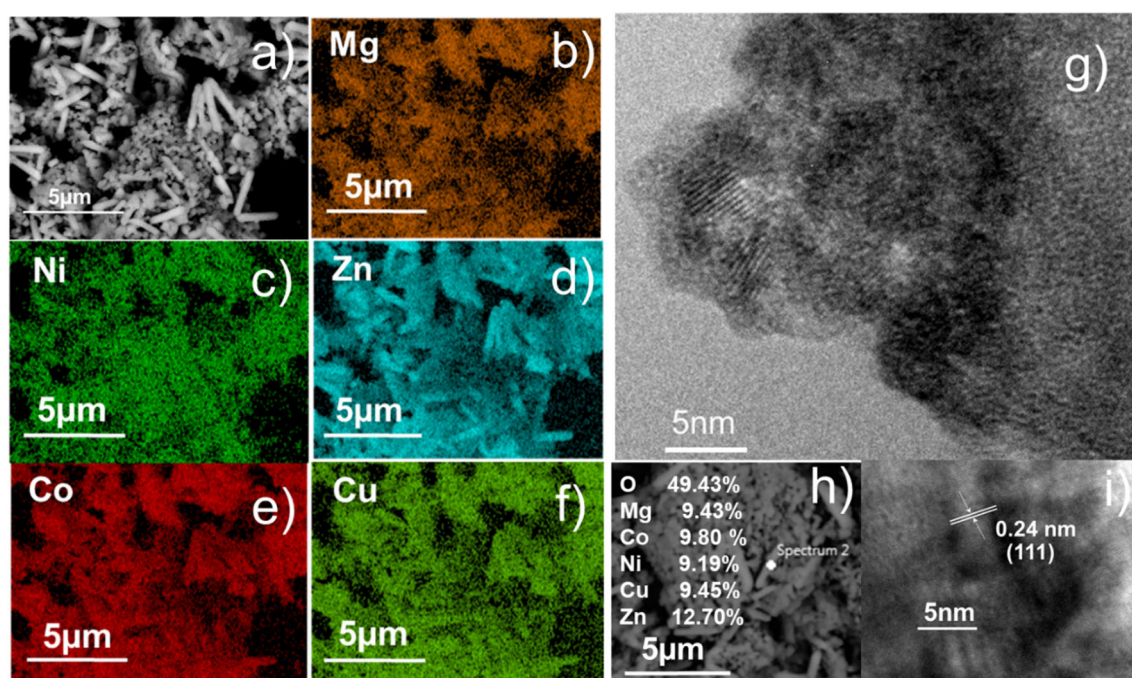
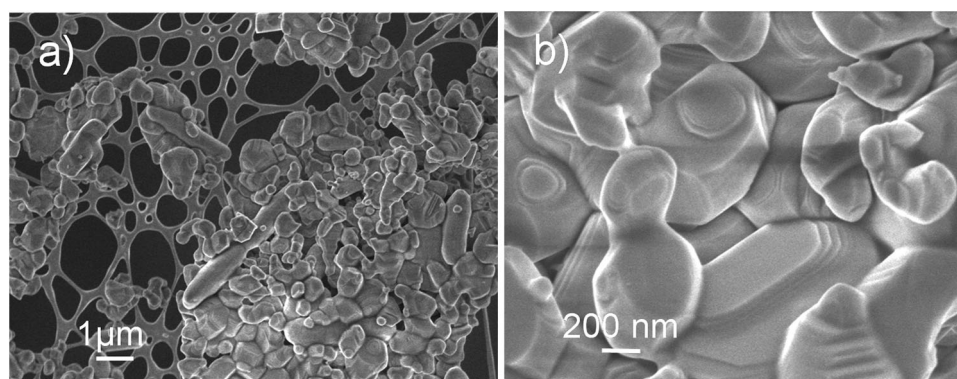


**Figure 3** Characterization of (CoCuMgNiZn)O powder: **a**, **h** SEM images, **b–f** EDX analysis of Mg, Ni, Zn, Co, Cu, **g**, **i** TEM images.

0.241 nm (Fig. 3i), which corresponds to the typical interplanar spacing of the (111) plane in (CoCuMgNiZn)O and is consistent with the XRD data.

Prior to investigate the electrochemical behavior of double-coated cathodes, some control experiments were carried out to qualitatively reveal the interaction between HEO and LiPSs. Adsorption experiments were performed by directly adding HEO particles into the Li<sub>2</sub>S<sub>6</sub> solution; the results are depicted in Fig. S1 of the Supporting Information. The Li<sub>2</sub>S<sub>6</sub> solution was initially dark yellow and became almost transparent by adding HEO powder after 12 h. The UV–vis adsorption spectra of the pristine Li<sub>2</sub>S<sub>6</sub> solution show three UV absorption bands in the 310–350 nm, 400–450 nm and 550–650 nm regions.

The strong absorption of S<sub>6</sub><sup>2−</sup> is detected at around 310 nm [43], while weaker bands are noticed around 420 nm (S<sub>4</sub><sup>2−</sup>) and 610 nm (S<sub>3</sub><sup>2−</sup>) [44]. These characteristic bands of Li<sub>2</sub>S<sub>6</sub> disappear when the solution is exposed to HEO powder, only a weak peak in the region from 300 to 400 nm results from the interaction between HEO and Li<sub>2</sub>S<sub>6</sub>, enlightening HEO ability to adsorb LiPSs [45].

Furthermore, additional evidence of the chemical interaction between HEO and Li<sub>2</sub>S<sub>6</sub> is provided by XPS analysis of HEO powder before and after the Li<sub>2</sub>S<sub>6</sub> adsorption test, and these results are shown in Fig. S2 of the Supporting Information. The most relevant interactions are observed in the high-resolution spectra of Ni2p, Mg1s and Zn2p [23]. The core peak



of Ni2p of HEO can be fitted into two spin–orbit doublets and two shake-up satellites. The symmetrical shape of the main peaks in Ni2p and the intense satellite peak at high binding energy indicate that nickel exists both as  $\text{Ni}^{2+}$  and  $\text{Ni}^{3+}$  in the HEO material [34]. After the  $\text{Li}_2\text{S}_6$  adsorption test, all peaks shift of about  $\approx 0.40$  eV toward higher binding energies (Fig. S2a). The shift shows that the environment around the surface of nickel is altered, indicating a chemical interaction between nickel and  $\text{Li}_2\text{S}_6$  [23]. Moreover, the high-resolution spectra of Mg1s and Zn2p show similar shifts toward higher binding energy of 0.4 eV and 0.5 eV, respectively (Fig. S2c,d). These results can be attributed to the electropositive nature of magnesium and zinc, which forces electrons away from the metal core in the LiPSs environment, resulting in the increase in the binding energy [46]. Figure S2b reports the high-resolution O1s spectra, which can be de-convoluted into three peaks [47]. The peak at 529.3 eV refers to lattice oxygen, arising from the ionic metal–oxygen bond. The peak at 531.3 eV is due to adsorbed oxygen species, and the peak at 532.6 eV is due to –OH from adsorbed moisture in HEO. All peaks shift 0.3 eV toward higher binding energies after the HEO is put in contact with the  $\text{Li}_2\text{S}_6$ . In this regard, by DFT calculations, Zheng et al. [23] postulated an interaction between oxygen species of HEO and lithium of LiPSs, due to the interfacial affinity between HEO and LiPSs. In Fig. S2b, the 0.3 eV shift in binding energy is small and the peak intensities do not change much from the O1s of pristine HEO; accordingly, a chemical bond between lithium polysulfides and oxygen is unlikely to form. To sum up, XPS analysis suggests that the major contribution to the absorption of  $\text{Li}_2\text{S}_6$  comes from the multi-cation system in HEO material.

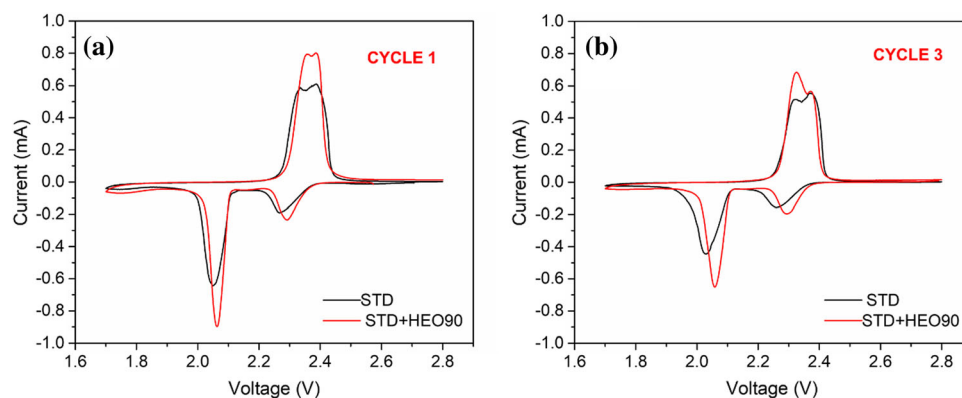
### Electrochemical characterization

The accelerated LiPSs redox reaction is firstly studied by cyclic voltammetry (CV) measurements using both STD and STD + HEO90 cathodes. This electrochemical test was performed only on these two electrode compositions since the main purpose of this characterization was to investigate the effect of the double layer of HEO on the reactions and kinetics of Li–S cells. Consequently, it is clear that maximizing the percentage of HEO in the double layer allows highlighting the role of HEO in this sense.

As shown in Fig. 4, the CV profiles display the typical two pairs of redox peaks, due to the cathodic reduction of S to long-chain LiPSs (at 2.27 V) and further transformation of the long-chain LiPSs into lower-order  $\text{Li}_2\text{S}_2$  and  $\text{Li}_2\text{S}$  (at 2.05 V). The two anodic oxidation peaks account for the oxidation of  $\text{Li}_2\text{S}$  to LiPSs and sulfur (at 2.34 and 2.38 V), respectively. As a matter of fact, the STD cathode (Fig. 4a, b) shows broader cathodic peaks with lower intensities than those of STD + HEO90 cathode, which is consistent with slower redox kinetics of LiPSs for both liquid/liquid and liquid/solid transformations. The CV curves highlight that HEOs mostly exert their influence on the conversion of short chain lithium polysulfides ( $\text{Li}_2\text{S}_x$ ,  $1 < x < 4$ ) to final  $\text{Li}_2\text{S}$ , since the reduction peak at 2.06 V and the oxidation peak at 2.35 V are more intense than those of the STD cathode. The onset potentials are shown in Table S1 in the Supporting Information, together with the peak potentials. The onset potentials were determined following the method proposed by Yuan et al. [48], and the differential CV curves are reported in Fig. S3 c,d in the Supporting Information. As depicted in Table S1, incorporation of HEO layer slightly increases the onset potentials of the reduction of both S and LiPSs, due to faster kinetics promoted by HEO. In particular, for STD cathode, a shift to lower potentials of the reduction peaks is observed from the 2<sup>nd</sup> cycle onward (Fig. 4b, S3a) These differences between the first and the following cycles reflect some redistribution of active sulfur in the STD to a less stable state, whereas the overlapping peak positions in the CV of STD + HEO90 indicate highly reversible electrochemical reaction (Fig. S3b).

To further probe the effect of HEO double-coated cathode on the redox kinetics of soluble intermediate LiPSs, CV measurements were performed at different scan rates. As shown in Fig. S4 in the Supporting Information, the linear relationship between the redox peak currents with the square root of scan rate involves that the diffusion process of LiPSs is the rate-determining step. The slopes of curves in Fig. S4 c,d,e are positively correlated with the corresponding  $\text{Li}^+$  diffusion [49] and the larger slope observed for the STD + HEO electrode, compared to that of the STD one, implies faster diffusion processes in the double-coated cathode. In particular, HEO enhances the transformation of the soluble  $\text{Li}_2\text{S}_4$  to the insoluble  $\text{Li}_2\text{S}$  (peak II). The poor capability of the STD to

**Figure 4** CV measurements performed at the scan rate of  $0.01 \text{ mV s}^{-1}$  in the voltage range of 1.7–2.8 V versus  $\text{Li}^+/\text{Li}$ : **a** STD cathode and double-coated cathode (STD + HEO90) first CV cycle; **b** third CV cycle.



capture LiPSs could be the reason for the lower diffusivity [50].

The aforementioned activity of the HEO materials in the Li-S cell is further demonstrated by galvanostatic charge/discharge at C/10 (first 3 cycles) followed by long-term galvanostatic cycling at C/5, which are used to evaluate the double-layer contribution and the effect of the layer composition. It was decided to further investigate this aspect by testing cathodes with two different HEO contents in the double layer (80%  $\text{wt}$  and 90%  $\text{wt}$ ), to better understand which composition could actually maximize the benefits of HEO materials, previously confirmed by the results of the CVs, and at the same time to balance their low electronic conductivity ( $10^{-8} \text{ S cm}^{-1}$ ) [27]. All potentials are intended versus  $\text{Li}^+/\text{Li}$ . As shown in Fig. 5, the STD cell displays an initial capacity of 778 mAh/g at C/10, while those of STD + HEO90 and STD + HEO80 cells are 1173 mAh/g and 1175 mAh/g, respectively. As seen, HEO double-layer allows to achieve higher specific capacity than the STD as a result of more efficient sulfur utilization. Addition of 10 wt % carbon in the double layer (STD + HEO80) does not affect the capacity values at C/10, which is the same in both STD + HEO80 and STD + HEO90 cells. Thus, the capacity at low current regime is entirely due to the presence of the HEO in the double-layer. After 250 cycles at C/5, the specific capacity of STD + HEO90 and STD + HEO80 is 528 mAh/g and 650 mAh/g, respectively. The capacity retention is 61% for STD + HEO90 and 69% for STD + HEO80, pertaining the value at the initial cycle at C/5 and after 250 cycles at the same current regime. The differences in the capacity retention between these cells are mainly due to the higher conductivity of the double layer in STD + HEO80 with additional 10 wt % carbon.

Indeed, 16% capacity loss is observed by increasing the C rate from C/10 to C/5 in STD + HEO90 (Fig. 5c), whereas only 7% is observed in STD + HEO80 cell (Fig. 5d), which means a better distribution of the insulating sulfur on the conductive carbon in STD + HEO80 cathode that improves the performance at higher current rates. Therefore, addition of 10wt % C in the double layer has the only effect of improving the capacity retention at C/5, which translates into higher capacity after 250 cycles. However, it is worth noting that STD + HEO90 retains 45% of its initial capacity after 500 cycles at C/5 (Fig. S5 of the Supporting Information), whereas the STD cell loses 61% of its initial capacity after only 250 cycles (Fig. 5a,b).

These results show that the STD + HEO90 maintains stable long-term cycling; moreover, the coulombic efficiency is approximately constant at 98.7% within 500 cycles at C/5, which means limited side reactions in STD + HEO90 cell.

The derivative-voltage profiles ( $dQ/dV$  vs  $V$ ) at different cycle numbers at C/5 (Fig. 6) highlight that STD + HEO90 and STD + HEO80 cathodes induce higher contribution to the lower voltage reduction reaction due to the conversion of short-chain LiPSs to  $\text{Li}_2\text{S}$  final product. In fact, the peaks at 2.05 V (in reduction) and 2.25 V (in oxidation) have higher intensity than those of the STD cathode, consistently to the trend observed in the CV measurements. In general, the derivative-voltage profiles comparison confirms higher process reversibility for the double-layer cathodes, explained by the active role of HEO in the LiPSs conversion. To further analyze the capacity characteristics of the double layer with respect to STD cathode, the capacity contribution from the upper-plateau discharge capacity ( $Q_1$ ) and the lower-plateau discharge capacity ( $Q_2$ ) were obtained and the

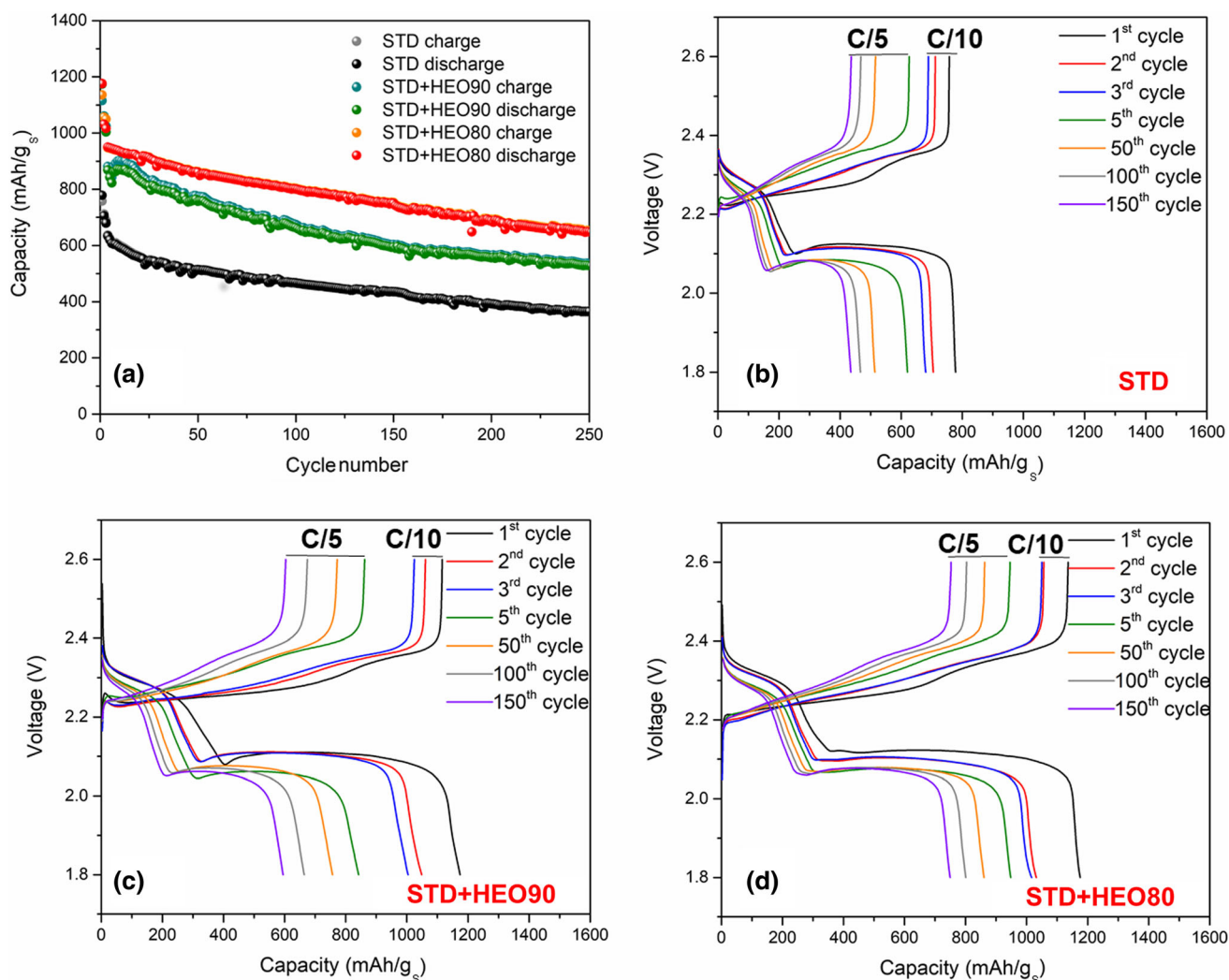


**Figure 5** a Long-term cycling performance of STD, STD + HEO90 and STD + HEO80 cells: first three cycles at C/10 followed by cycling at C/5. Capacity versus voltage plots for:

b STD cell, c STD + HEO90 cell, d STD + HEO80 cell. Sulfur loading: 1.0 mg/cm<sup>2</sup>, electrolyte to sulfur ratio: 10  $\mu$ L/mg.

$Q_2/Q_1$  ratio versus cycle number is reported in Fig. 6d for both STD and STD + HEO90 cells. In this respect, Manthiram et al. [51] reported that the theoretical  $Q_2/Q_1$  ratio should be equal to 3, since the theoretical capacity attributed to  $Q_1$  is 419 mAh/g and that of  $Q_2$  is 1256 mAh/g. In actual Li-S cells, however, shuttling effects and/or inappropriate reactions lower this ratio far below the theoretical. As can be seen in Fig. 6d the STD + HEO90 electrode shows higher  $Q_2/Q_1$  values of  $\sim 2.3$  at C/10 and  $\sim 2.1$  at C/5 over 100 cycles than the STD ( $\sim 2.2$  at C/10 and  $\sim 1.8$  at C/5), which means that the double layer with HEO exerts more efficient conversion of LiPSs and better sulfur utilization over 100 cycles at C/5.

Figure S6 a-c reports the EIS responses for the pristine cathodes, and after eight CV cycles, the EIS results were fitted with the equivalent circuit shown in Fig. S6d.

For all three cathodes, a semicircle at high frequencies is observed which intersects the  $Z_{Re}$  axis in  $R_s$  and then at  $R_s + R_{ct}$ , the semicircle diameter represents the charge transfer resistances ( $R_{ct}$ ). For the three pristine electrodes, this value is around 36  $\Omega$ , while after eight CV cycles, it slightly increases for the double-layer electrodes, though it remains stable for the standard (within the experimental error). This increment is more noticeable with the increase of the amount of HEO in the double layer. After eight CV cycles, the change of  $R_{ct}$  is associated

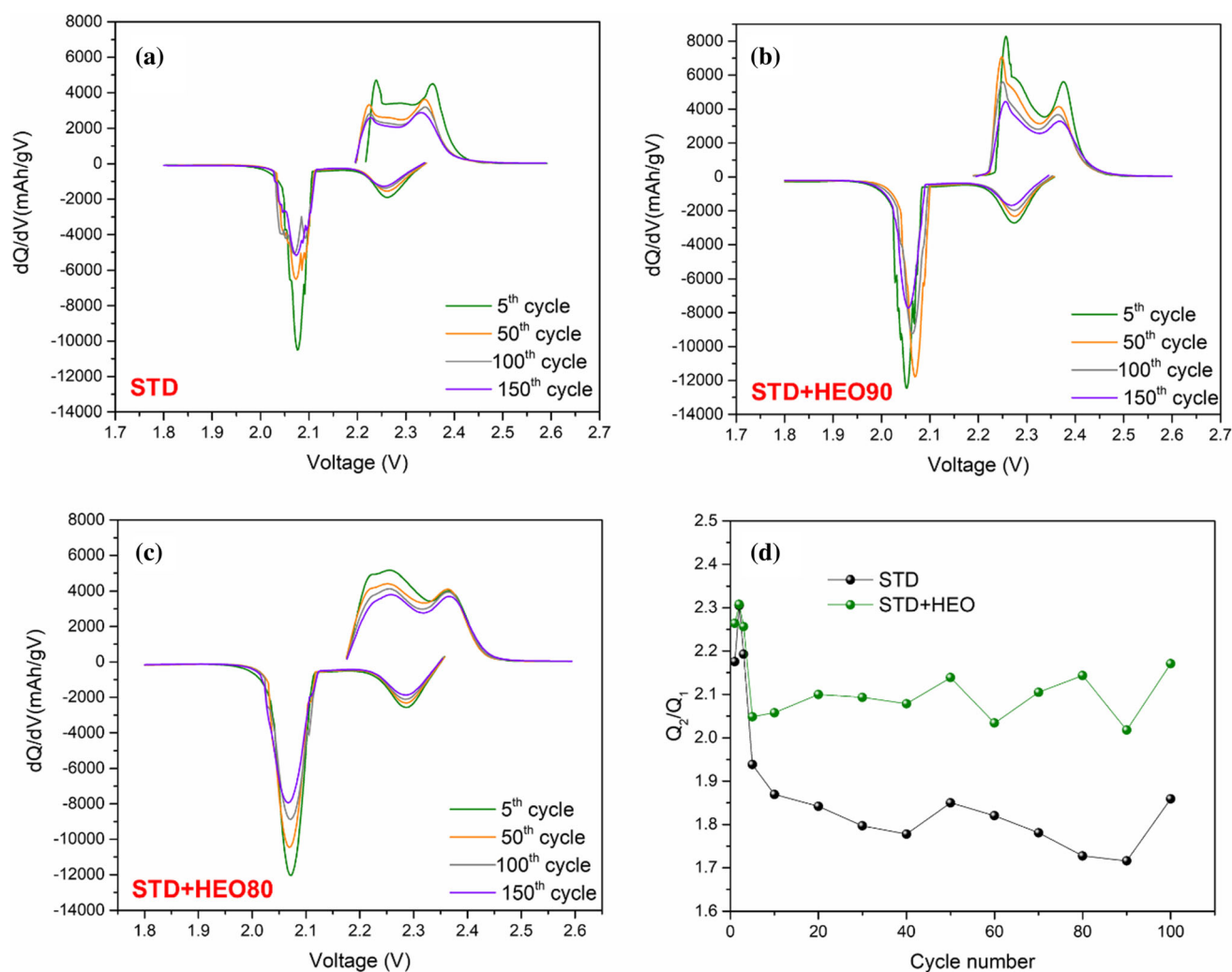


**Figure 6** Relative  $dQ/dV$  versus  $V$  plot derived from galvanostatic discharge/charge at  $C/5$  reported in Fig. 5: **a** STD, **b** STD + HEO90, **c** STD + HEO80 and **d**  $Q_2/Q_1$  plot versus cycle number for STD and STD + HEO90 cells.

with the formation of more resistive cathode electrolyte interface (CEI) on the HEO-modified electrodes, and the higher increment is observed for STD + HEO90 cathode. At lower frequencies, a linear dependence between  $Z_{Re}$  and  $-Z_{Im}$  is observed, this frequency range contains the long constant time processes, as the ion diffusion of reactive ions and non-reactive ions which can accumulate in the electrode pores. This is fitted with a CPE (shown in the equivalent circuit as  $W$  in Fig. S6d). By comparing with the pristine cathodes, a more capacitive behavior for STD + HEO80 and STD + HEO90 electrodes is observed, as the responses have a higher slope, while the STD cathode has less capacitive behavior since the slope is lower. After eight CV cycles, the behavior becomes less capacitive and the slope at low frequencies decreases. Furthermore, there are no

significant differences between STD + HEO80 and STD + HEO90. In summary, the double-layer cathode shows a  $R_{ct}$  increment after cycling, that is mostly associated with a more resistive CEI due to the presence of the second layer.

Additionally, the rate capability of cells was evaluated at various rates from  $C/10$  to  $1C$ , as shown in Fig. 7. In this case, the STD + HEO80 cell displayed the best performance, from the initial capacity of about 1000 mAh/g at  $C/10$  to capacity values of 930, 840 and 520 mAh/g at  $C/5$ ,  $C/2$  and  $1C$ , respectively. The results of the rate capability highlight that negligible benefits are achieved at high  $C$  rates with STD + HEO90 cell compared to the STD one, in which 70 wt % S is simply mixed with 20 wt % C and 10% of binder by ball-milling. In fact, the voltage hysteresis between charge and discharge curves



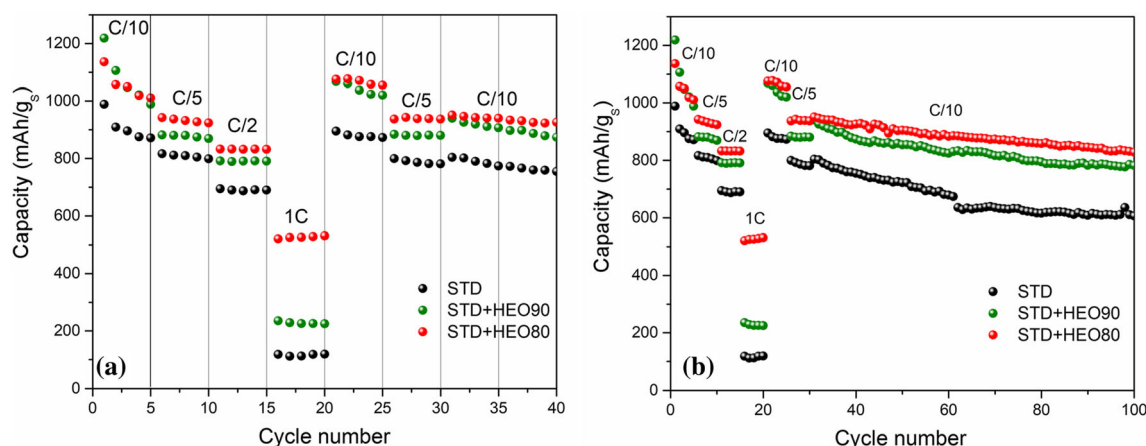


**Figure 7** **a** Charge and discharge curves under different current rates for STD, STD + HEO80 and STD + HEO90 cells; **b** specific discharge capacity versus cycle number at different

current rates and long-term cycling at C/10. Sulfur loading:  $1.0 \text{ mg/cm}^2$ , electrolyte to sulfur ratio:  $10 \text{ }\mu\text{L/mg}$ .

showed high overpotential for STD + HEO90 particularly at C/2 (Fig. S7c of the Supporting Information), mostly due to the low conductivity of S ( $5 \times 10^{-30} \text{ S cm}^{-1}$ ) and of HEO in the electrode. However, and unlike the STD cell, when the C rate is reduced to C/10 the voltage hysteresis of the STD + HEO90 cell abruptly decreases (Fig. S7d) and most of the reversible capacity,  $\sim 900 \text{ mAh/g}$ , is recovered with very slow capacity rate degradation of 0.15% per cycle from 45 to 100th cycles, which confirms the synergistic affinity of multi-element in HEO to LiPSs, resulting in stable cycling performance (Fig. 7b).

## Conclusions

In summary, a smart and rapid preparation of Li-S battery electrode with a HEO layer coated on the sulfur cathode has been developed, which is suitable for large-scale production and exhibits a favorable electrochemical performance and steady cyclic efficiency. In particular, when compared with the traditional melt infusion process, the double-layer approach allows to better discriminate the role of HEO, since the sulfur is simply physically mixed with the carbon black and the oxide powders. This procedure is particularly effective for long cycling performance at low C rates (C/10), while additional 10 wt % C in the double layer is required to ensure appreciable rate capability. Furthermore, a novel and simple synthesis strategy by microwave irradiation has been proposed to produce HEO materials. This

experimental procedure presents several advantages when compared with others such as flame pyrolysis or typical hydrothermal route: It is safer than the former and dramatically faster than the latter. We have demonstrated the synergistic contribution of the multi-elements in HEO to absorb LiPSs, *i.e.*, one of the main issues regarding Li-S batteries, and the improvement of the electrochemical kinetics.

Overall, the material is electrochemically stable and the compositional uniformity and consistency in charge/discharge processes ensured efficient and stable Li-S cell operation, with a coulombic efficiency approximately constant at 98.7% within 500 cycles at C/5. The cycling results clearly highlight the fact that the presence of HEO is beneficial to the performances of the Li-S cell, since the cycling stability and specific capacity are higher than those exhibited by the standard sulfur electrode.

In conclusion, our findings can significantly contribute to counter the unwanted effects caused by LiPSs, bringing Li-S batteries closer to the industrial scalability also leveraging on rapid and sustainable preparation processes, such as the microwave-based one presented in this study.

## Funding

Open access funding provided by Politecnico di Torino within the CRUI-CARE Agreement.

**Supplementary Information:** The online version contains supplementary material available at <http://doi.org/10.1007/s10853-022-07625-7>.

**Open Access** This article is licensed under a Creative Commons Attribution 4.0 International License, which permits use, sharing, adaptation, distribution and reproduction in any medium or format, as long as you give appropriate credit to the original author(s) and the source, provide a link to the Creative Commons licence, and indicate if changes were made. The images or other third party material in this article are included in the article's Creative Commons licence, unless indicated otherwise in a credit line to the material. If material is not included in the article's Creative Commons licence and your intended use is not permitted by statutory regulation or exceeds the permitted use, you will need to obtain permission directly from the copyright holder. To view a copy of this licence, visit <http://creativecommons.org/licenses/by/4.0/>.

## References

- [1] Pang Q, Kundu D, Nazar LF (2016) A graphene-like metallic cathode host for long-life and high-loading lithium–sulfur batteries. *Mater Horiz* 3:130–136. <https://doi.org/10.1039/C5MH00246J>
- [2] Duffner F, Kronemeyer N, Tübke J et al (2021) Post-lithium-ion battery cell production and its compatibility with lithium-ion cell production infrastructure. *Nat Energy* 6:123–134. <https://doi.org/10.1038/s41560-020-00748-8>
- [3] Wild M, O'Neill L, Zhang T et al (2015) Lithium sulfur batteries, a mechanistic review. *Energy Environ Sci* 8:3477–3494. <https://doi.org/10.1039/C5EE01388G>
- [4] Barghamadi M, Kapoor A, Wen C (2013) A review on Li–S batteries as a high efficiency rechargeable lithium battery. *J Electrochem Soc* 160:A1256–A1263. <https://doi.org/10.1149/2.096308jes>
- [5] Yuan H, Peng H-J, Li B-Q et al (2019) Conductive and catalytic triple-phase interfaces enabling uniform nucleation in high-rate lithium–sulfur batteries. *Adv Energy Mater* 9:1802768–1802776. <https://doi.org/10.1002/aenm.201802768>
- [6] Velasco JJ, Vélez P, Zoloff Michoff ME et al (2021) Role of the solvent in the activation of Li<sub>2</sub>S as cathode material: a DFT study. *J Phys Condens Matter* 33:344003–344014. <https://doi.org/10.1088/1361-648X/ac08b9>
- [7] Zhang L, Wang Y, Niu Z, Chen J (2019) Advanced nanostructured carbon-based materials for rechargeable lithium–sulfur batteries. *Carbon* 141:400–416. <https://doi.org/10.1016/j.carbon.2018.09.067>
- [8] Liu X, Huang J-Q, Zhang Q, Mai L (2017) Nanostructured metal oxides and sulfides for lithium–sulfur batteries. *Advanced Materials* 29:1601759–1601784. <https://doi.org/10.1002/adma.201601759>
- [9] Su Y-S, Manthiram A (2012) Lithium–sulphur batteries with a microporous carbon paper as a bifunctional interlayer. *Nat Commun* 3:1–6. <https://doi.org/10.1038/ncomms2163>
- [10] Deng N, Liu Y, Li Q et al (2019) Functional mechanism analysis and customized structure design of interlayers for high performance Li–S battery. *Energy Storage Mater* 23:314–349. <https://doi.org/10.1016/j.ensm.2019.04.042>
- [11] García-Soriano FJ, Para ML, Luque GL et al (2020) Improving the polysulfide barrier by efficient carbon nanofibers coating on separator/cathode for Li–S batteries. *J Solid State Electrochem* 24:2341–2351. <https://doi.org/10.1007/s10008-020-04749-1>
- [12] Zhao M, Peng Y-Q, Li B-Q et al (2021) Regulation of carbon distribution to construct high-sulfur-content cathode in lithium–sulfur batteries. *J Energy Chem* 56:203–208. <https://doi.org/10.1016/j.jechem.2020.07.054>
- [13] Sun W, Ou X, Yue X et al (2016) A simply effective double-coating cathode with MnO<sub>2</sub> nanosheets/graphene as functionalized interlayer for high performance lithium-sulfur batteries. *Electrochim Acta* 207:198–206. <https://doi.org/10.1016/j.electacta.2016.04.135>
- [14] Fang J, Qin F, Li J et al (2015) Improved performance of sulfur cathode by an easy and scale-up coating strategy. *J Power Sour* 297:265–270. <https://doi.org/10.1016/j.jpowsour.2015.06.153>
- [15] Versaci D, Cozzarin M, Amici J et al (2021) Influence of synthesis parameters on g-C<sub>3</sub>N<sub>4</sub> polysulfides trapping: a systematic study. *Appl Mater Today* 25:101169–101182. <https://doi.org/10.1016/j.apmt.2021.101169>
- [16] Liu Z, Liu B, Guo P et al (2018) Enhanced electrochemical kinetics in lithium-sulfur batteries by using carbon nanofibers/manganese dioxide composite as a bifunctional coating on sulfur cathode. *Electrochim Acta* 269:180–187. <https://doi.org/10.1016/j.electacta.2018.02.160>
- [17] Liu M, Deng N, Ju J et al (2019) A review: electrospun nanofiber materials for lithium–sulfur batteries. *Adv Funct Mater* 29:1905367–1905401. <https://doi.org/10.1002/adfm.201905467>
- [18] Kong L, Chen X, Li B-Q et al (2018) A bifunctional perovskite promoter for polysulfide regulation toward stable lithium–sulfur batteries. *Adv Mater*

- 30:1705219–1705226. <https://doi.org/10.1002/adma.201705219>
- [19] Sun Q, Xi B, Li J-Y et al (2018) Nitrogen-doped graphene-supported mixed transition-metal oxide porous particles to confine polysulfides for lithium–sulfur batteries. *Adv Energy Mater* 8:1800595–1800605. <https://doi.org/10.1002/aenm.201800595>
- [20] Fan Q, Liu W, Weng Z et al (2015) Ternary hybrid material for high-performance lithium–sulfur battery. *J Am Chem Soc* 137:12946–12953. <https://doi.org/10.1021/jacs.5b07071>
- [21] Wu F, Pollard TP, Zhao E et al (2018) Layered LiTiO<sub>2</sub> for the protection of Li<sub>2</sub>S cathodes against dissolution: mechanisms of the remarkable performance boost. *Energy Environ Sci* 11:807–817. <https://doi.org/10.1039/C8EE00419F>
- [22] Zhang Y, Zhao Y, Yermukhambetova A et al (2013) Ternary sulfur/polyacrylonitrile/Mg<sub>0.6</sub>Ni<sub>0.4</sub>O composite cathodes for high performance lithium/sulfur batteries. *J Mater Chem A* 1:295–301. <https://doi.org/10.1039/C2TA00105E>
- [23] Zheng Y, Yi Y, Fan M et al (2019) A high-entropy metal oxide as chemical anchor of polysulfide for lithium–sulfur batteries. *Energy Storage Mater* 23:678–683. <https://doi.org/10.1016/j.ensm.2019.02.030>
- [24] Rost CM, Sachet E, Borman T et al (2015) Entropy-stabilized oxides. *Nat Commun* 6:1–8. <https://doi.org/10.1038/ncomms9485>
- [25] Tavani F, Fracchia M, Pianta N et al (2020) Multivariate curve resolution analysis of operando XAS data for the investigation of the lithiation mechanisms in high entropy oxides. *Chem Phys Lett* 760:137968–137974. <https://doi.org/10.1016/j.cplett.2020.137968>
- [26] Sarkar A, Velasco L, Wang D et al (2018) High entropy oxides for reversible energy storage. *Nat Commun* 9:1–9. <https://doi.org/10.1038/s41467-018-05774-5>
- [27] Sarkar A, Wang Q, Schiele A et al (2019) High-entropy oxides: fundamental aspects and electrochemical properties. *Adv Mater* 31:1806236–1806245. <https://doi.org/10.1002/adma.201806236>
- [28] Yuan K, Tu T, Shen C et al (2022) Self-ball milling strategy to construct high-entropy oxide coated LiNi<sub>0.8</sub>-Co<sub>0.1</sub>Mn<sub>0.1</sub>O<sub>2</sub> with enhanced electrochemical performance. *J Adv Ceram* 11:882–892. <https://doi.org/10.1007/s40145-022-0582-6>
- [29] Tian LY, Zhang Z, Liu S et al (2021) High-entropy spinel oxide nanofibers as catalytic sulfur hosts promise the high gravimetric and volumetric capacities for lithium–sulfur batteries. *Energy Environ Mater* 645–654. <https://doi.org/10.1002/eem2.12215>
- [30] Sarkar A, Breitung B, Hahn H (2020) High entropy oxides: the role of entropy, enthalpy and synergy. *Scripta Mater* 187:43–48. <https://doi.org/10.1016/j.scriptamat.2020.05.019>
- [31] Qiu N, Chen H, Yang Z et al (2019) A high entropy oxide (Mg<sub>0.2</sub>Co<sub>0.2</sub>Ni<sub>0.2</sub>Cu<sub>0.2</sub>Zn<sub>0.2</sub>O) with superior lithium storage performance. *J Alloys Compd* 777:767–774. <https://doi.org/10.1016/j.jallcom.2018.11.049>
- [32] Hong W, Chen F, Shen Q et al (2019) Microstructural evolution and mechanical properties of (Mg Co, Ni, Cu, Zn)O high-entropy ceramics. *J Am Ceram Soc* 102:2228–2237. <https://doi.org/10.1111/jace.16075>
- [33] Kheradmandfard M, Kashani-Bozorg SF, Noori-Alfesharaki AH et al (2018) Ultra-fast, highly efficient and green synthesis of bioactive forsterite nanopowder via microwave irradiation. *Mater Sci Eng C* 92:236–244. <https://doi.org/10.1016/j.msec.2018.06.026>
- [34] Kheradmandfard M, Minouei H, Tsvetkov N et al (2021) Ultrafast green microwave-assisted synthesis of high-entropy oxide nanoparticles for Li-ion battery applications. *Mater Chem Phys* 262:124265–124275. <https://doi.org/10.1016/j.matchemphys.2021.124265>
- [35] Biesuz M, Spiridigliozzi L, Dell'Agli G et al (2018) Synthesis and sintering of (Mg Co, Ni, Cu, Zn)O entropy-stabilized oxides obtained by wet chemical methods. *J Mater Sci* 53:8074–8085. <https://doi.org/10.1007/s10853-018-2168-9>
- [36] Nguyen TX, Patra J, Chang JK, Ting JM (2020) High entropy spinel oxide nanoparticles for superior lithiation–delithiation performance. *J Mater Chem A* 8:18963–18973. <https://doi.org/10.1039/d0ta04844e>
- [37] Nguyen TX, Tsai CC, Patra J et al (2022) Co-free high entropy spinel oxide anode with controlled morphology and crystallinity for outstanding charge/discharge performance in Lithium-ion batteries. *Chem Eng J* 430:132658–132667. <https://doi.org/10.1016/j.cej.2021.132658>
- [38] Sarkar A, Djenadic R, Usharani NJ et al (2017) Nanocrystalline multicomponent entropy stabilised transition metal oxides. *J Eur Ceram Soc* 37:747–754. <https://doi.org/10.1016/j.jeurceramsoc.2016.09.018>
- [39] Mao A, Xiang H-Z, Zhang Z-G et al (2019) Solution combustion synthesis and magnetic property of rock-salt (Co<sub>0.2</sub>Cu<sub>0.2</sub>Mg<sub>0.2</sub>Ni<sub>0.2</sub>Zn<sub>0.2</sub>)O high-entropy oxide nanocrystalline powder. *J Magn Magn Mater* 484:245–252. <https://doi.org/10.1016/j.jmmm.2019.04.023>
- [40] Berardan D, Meena AK, Franger S et al (2017) Controlled Jahn-Teller distortion in (MgCoNiCuZn)O-based high entropy oxides. *J Alloys Compd* 704:693–700. <https://doi.org/10.1016/j.jallcom.2017.02.070>
- [41] Lal MS, Sundara R (2019) High entropy oxides—a cost-effective catalyst for the growth of high yield carbon nanotubes and their energy applications. *ACS Appl Mater Interfaces* 11:30846–30857. <https://doi.org/10.1021/acsami.9b08794>

- [42] Evers S, Yim T, Nazar LF (2012) Understanding the nature of absorption/adsorption in nanoporous polysulfide sorbents for the Li–S battery. *J Phys Chem C* 116:19653–19658. <https://doi.org/10.1021/jp304380j>
- [43] Zhao X, Wang J, Sun X et al (2021) Hierarchical porous carbon with nano-MgO as efficient sulfur species micro-reactors for lithium-sulfur battery. *J Electrochem Soc* 168:40506–40514. <https://doi.org/10.1149/1945-7111/abed2a>
- [44] Barchasz C, Molton F, Duboc C et al (2012) Lithium/sulfur cell discharge mechanism: an original approach for intermediate species identification. *Anal Chem* 84:3973–3980. <https://doi.org/10.1021/ac2032244>
- [45] Wang Y, Guo X, Chen C et al (2020) Alleviating the shuttle effect via bifunctional MnFe<sub>2</sub>O<sub>4</sub>/AB modified separator for high performance lithium sulfur battery. *Electrochim Acta* 354:136704. <https://doi.org/10.1016/j.electacta.2020.136704>
- [46] Ponraj R, Kannan AG, Ahn JH, Kim D-W (2016) Improvement of cycling performance of lithium–sulfur batteries by using magnesium oxide as a functional additive for trapping lithium polysulfide. *ACS Appl Mater Interfaces* 8:4000–4006. <https://doi.org/10.1021/acsami.5b11327>
- [47] Usharani NJ, Shringi R, Sanghavi H et al (2020) Role of size, alio-/multi-valency and non-stoichiometry in the synthesis of phase-pure high entropy oxide (Co, Cu, Mg, Na, Ni, Zn)O. *Dalton Trans* 49:7123–7132. <https://doi.org/10.1039/D0DT00958J>
- [48] Yuan Z, Peng H-J, Hou T-Z et al (2016) Powering lithium–sulfur battery performance by propelling polysulfide redox at sulfiphilic hosts. *Nano Lett* 16:519–527. <https://doi.org/10.1021/acs.nanolett.5b04166>
- [49] Liu Y-T, Han D-D, Wang L et al (2019) NiCo<sub>2</sub>O<sub>4</sub> nanofibers as carbon-free sulfur immobilizer to fabricate sulfur-based composite with high volumetric capacity for lithium–sulfur battery. *Adv Energy Mater* 9:1803477. <https://doi.org/10.1002/aenm.201803477>
- [50] Tao X, Wang J, Liu C et al (2016) Balancing surface adsorption and diffusion of lithium-polysulfides on non-conductive oxides for lithium–sulfur battery design. *Nat Commun* 7:11203. <https://doi.org/10.1038/ncomms11203>
- [51] Su YS, Fu Y, Cochell T, Manthiram A (2013) A strategic approach to recharging lithium-sulphur batteries for long cycle life. *Nat Commun* 4:1–8. <https://doi.org/10.1038/ncomms3985>

**Publisher's Note** Springer Nature remains neutral with regard to jurisdictional claims in published maps and institutional affiliations.